1 **Technical note: Measurement of chemically-resolved volume**

2 **equivalent diameter and effective density of particles by AAC-**

3 **SPAMS**

4 Long Peng[1,2], Lei Li[4], Guohua Zhang[1, 3*], Xubing Du[4], Xinming Wang[1, 3], Ping'an

5 Peng[1, 3], Guoying Sheng[1], Xinhui Bi[1, 3*]

7 [1] State Key Laboratory of Organic Geochemistry and Guangdong Provincial Key

8 Laboratory of Environmental Protection and Resources Utilization, Guangzhou

9 Institute of Geochemistry, Chinese Academy of Sciences, Guangzhou 510640, China

10 [2] University of Chinese Academy of Sciences, Beijing, 100049, China

11 [3] Guangdong-Hong Kong-Macao Joint Laboratory for Environmental Pollution and

12 Control, Guangzhou 510640, China

13 [4] Institute of Mass Spectrometer and Atmospheric Environment, Jinan University,

14 Guangzhou 510632, China

16 *Correspondence to: bixh@gig.ac.cn and zhanggh@gig.ac.cn

## Abstract

18     Size and effective density ($\rho_e$) are important properties of aerosol particles and are

19     related to their influences on human health and the global climate. The volume

20     equivalent diameter ($D_{ve}$) is an intrinsic property that is used to evaluate particle size.

21     $\rho_e$, defined as the ratio of particle density to a dynamic shape factor ($\chi$), is used to

22     characterize the physical property of a particle as an alternative to particle density.

23     However, it is still challenging to simultaneously characterize the $D_{ve}$ and $\rho_e$ of particles.

24     Here, we present a novel system that classifying particles with their aerodynamic

25     diameter ($D_a$) by aerodynamic aerosol classifiers (AAC) and determining their vacuum

26     aerodynamic diameter ($D_{va}$) by single particle aerosol mass spectrometry (SPAMS) to

27     achieve a measurement of $D_{ve}$ and $\rho_e$. The reliability of the AAC-SPAMS system for

28     accurately obtaining $D_{ve}$ and $\rho_e$ is verified based on the results that the deviation between

29     the measured values and the theoretical values is less than 4% for the size-resolved

30     spherical polystyrene latex (PSL). The AAC-SPAMS system is applied to characterize

31     the $D_{ve}$ and $\rho_e$ of $(NH_4)_2SO_4$ and $NaNO_3$ particles, suggesting that these particles are

32     aspherical and their $\rho_e$ are independent of particle size. Finally, the AAC-SPAMS

33     system is deployed in a field measurement, showing that it is a powerful technique to

34     characterize the chemically-resolved $D_{ve}$ and $\rho_e$ of particles in real time.

## 1. Introduction

35

36  Size and particle density ($\rho_p$) are critical parameters of aerosol particles in

37  quantifying the impact of aerosols on air quality, human health and global climate

38  change (Buseck and Posfai, 1999; Poschl, 2005; Pitz et al., 2003). Effective density ($\rho_e$)

39  has been adopted to characterize the physical property of a particle as an alternative to

40  $\rho_p$, since $\rho_p$ for aspherical aerosol particles is hardly measured (Sumlin et al., 2018;

41  Katrib et al., 2005). Size and $\rho_e$ govern the transport properties of a particle both in the

42  atmosphere and in the human respiratory system (Seinfeld and Pandis, 1998; Liu and

43  Daum, 2008) and directly/indirectly influence the potential of the particle to absorb or

44  reflect solar radiation (Tang, 1997; Zhao et al., 2019; Liu and Daum, 2008). $\rho_e$ can also

45  provide information concerning particle morphology (Yon et al., 2015) and serve as a

46  tracer for atmospheric processing (Guo et al., 2014; Yin et al., 2015; Liu et al., 2015).

47  However, the quantitative relationship between aerosol properties, namely, size and $\rho_e$,

48  and their effects on air quality, human health and global climate change is not yet well

49  understood, which is partly because important aerosol properties cannot be measured

50  by current techniques.

51  **Size.** Size is a fundamental property of particles, which can be parameterized by the

52  physical quantity of volume equivalent diameter ($D_{ve}$). Defined as the diameter of a

53  spherical particle with the same volume as the particle (DeCarlo et al., 2004), $D_{ve}$ is an

54  intrinsic physical quantity that can be used to evaluate the actual size of the particle.

55  However, to date, atmospheric science usually describes particle size by other diameter

56  definitions, such as the electric mobility diameter ($D_m$), aerodynamic equivalent

57    diameter ($D_a$) and vacuum aerodynamic equivalent diameter ($D_{va}$), whose relationships

58    with $D_{ve}$ are shown in Eqs. (1)-(3), respectively:

59
$$\frac{D_m}{C_c(D_m)} = \frac{D_{ve}}{C_c(D_{ve})} \chi_t, \qquad (1)$$

60
$$D_a = D_{ve} \sqrt{\frac{\rho_p C_c(D_{ve})}{\chi_t \cdot \rho_0 \cdot C_c(D_a)}}, \qquad (2)$$

61
$$D_{va} = \frac{\rho_p}{\rho_0} \frac{D_{ve}}{\chi_v}, \qquad (3)$$

62    where $C_c(D)$ is the Cunningham slip correction factor, $\chi_t$ and $\chi_v$ represent the aerosol

63    dynamic shape factor ($\chi$) in the transition regime and in the free-molecule regime,

64    respectively, and $\rho_0$ represents the unit density of 1.0 g/cm$^3$. From the definitions, it can

65    be seen that $D_m$, $D_a$, and $D_{va}$ are originally derived from $D_{ve}$, but in actuality, they do

66    not reflect the actual size of the particle. Meanwhile, $D_{ve}$ cannot be easily obtained,

67    which limits its application in the scientific community.

68        **Effective density.** At present, three definitions of $\rho_e$ are introduced in atmospheric

69    science (DeCarlo et al., 2004): the first definition ($\rho_e^I$) is the ratio of the measured

70    particle mass ($m_p$) to the particle volume ($V$) calculated assuming a spherical particle

71    with a diameter equal to the measured $D_m$; the second definition ($\rho_e^{II}$) is the ratio of $D_m$

72    and $D_{va}$; and the third definition ($\rho_e^{III}$) is the ratio of $\rho$ to $\chi$, all of which are expressed

73    in Eqs. (4)-(6), respectively.

74
$$\rho_e^I = \frac{6m_p}{\pi D_m^3} \qquad (4)$$

75
$$\rho_e^{II} = \frac{D_{va}}{D_m} \rho_0 \qquad (5)$$

76
$$\rho_e^{III} = \frac{\rho_p}{\chi} \qquad (6)$$

77    When the above equations are combined with Eqs. (1) and (3), the final forms of

78    $\rho_e^I$ and $\rho_e^{II}$ can be expressed as Eqs. (7) and (8), respectively:

79
$$\rho_e^{\mathrm{I}} = \frac{\rho}{\chi^3} \cdot \left(\frac{C_c(D_{ve})}{C_c(D_m)}\right)^3 \qquad (7)$$

80
$$\rho_e^{\mathrm{II}} = \frac{\rho}{\rho_0} \cdot \frac{C_c(D_{ve})}{\chi^2 \cdot C_c(D_m)} \qquad (8)$$

81 The detailed derivation will be presented in a separate paper, in which we demonstrate

82 that $\rho_e^I$ and $\rho_e^{II}$ have the inherent characteristics of decreasing with increasing particle

83 size. Therefore, it will introduce systemic error when assessing the particle impacts on

84 visibility, human health and climate from the physical quantities in $\rho_e^I$ and $\rho_e^{II}$. In

85 contrast, $\rho_e^{III}$ is independent of particle size. Previously, $\rho_e^{III}$ for the spherical particles

86 was derived from Mie modelling of the scattering signals collected by single particle

87 mass spectrometry (Moffet and Prather, 2005). However, there is no effective

88 technique to achieve the measurement of $\rho_e^{III}$ for aspherical particles. Thus, for

89 reference, the symbol $\rho_e$ in the following text refers to the definition of $\rho_e^{III}$.

90    The aim of the present work is to develop a method to obtain $D_{ve}$ and $\rho_e$. The

91 established system of an aerodynamic aerosol classifier (AAC)-single particle aerosol

92 mass spectrometry (SPAMS) is capable of characterizing the $D_a$ and $D_{va}$ of particles,

93 which can be applied to theoretically derive $D_{ve}$ and $\rho_e$. To verify the reliability of the

94 AAC-SPAMS system, we apply it to measure the $D_{ve}$ and $\rho_e$ of the spherical particles

95 of polystyrene latex (PSL). The results are in good agreement with the theoretical values.

96 Finally, the AAC-SPAMS system is applied to measure the $D_{ve}$ and $\rho_e$ for $(NH_4)_2SO_4$

97 and $NaNO_3$ particles and for the chemically-resolved atmospheric particles.

98

99 **2. Experimental section**

100 **2.1 Measurement system**

101    Figure 1 shows a schematic diagram of the AAC-SPAMS system. The particles are

102    first dried by a diffusion drying tube (TSI 9302, USA), classified by AAC (Cambustion

103    Ltd., UK) based on the aerodynamic diameters $D_a$, and then transported into SPAMS in

104    which the $D_{va}$ and the mass spectra of individual particles are obtained. The working

105    principle of the AAC is described in detail elsewhere (Tavakoli and Olfert, 2013). AAC

106    consists of two coaxial cylinders that rotate at the same rotational speed. Polydisperse

107    particles enter into the space between the cylinders (i.e., classification column) and

108    experience a centrifugal force that causes them to move toward the outer cylinder. The

109    particles to be classified can leave the classification column with the particle-free sheath

110    flow and finally exit the AAC with the sample flow. Thus, the $D_a$ values of classified

111    particles can be derived from their relationship with their relaxation time ($\tau$), as shown

112    in Eq. (9):

113
$$\tau = \frac{C_C(D_a) \cdot \rho_0 \cdot D_a^2}{18\mu} \tag{9}$$

114    where $\mu$ is the gas dynamic viscosity. Particles with large relaxation times impact and

115    adhere to the outer cylinder, while particles with small relaxation times exit the

116    classifier with the exhaust flow.

117     Detailed information about the operation of SPAMS (Hexin Analytical Instrument

118    Co., Ltd., China) is described elsewhere (Li et al., 2011). Briefly, the particles are

119    introduced into the vacuum system through a 0.1 mm critical orifice and are gradually

120    collimated into a beam in the aerodynamic lens. Two continuous diode Nd:YAG laser

121    beams (532 nm) are used to aerodynamically size the particles, which are subsequently

122    desorbed/ionized by a pulsed laser (266 nm) that is triggered based on the velocity of a

123   specific particle. The generated positive and negative ions are recorded with the

124   corresponding particle size. The $D_{va}$ of the particle is related to the transit time between

125   the two laser beams (532 nm) in SPAMS, which can be obtained by using a calibration

126   curve generated from the measured transit times of a PSL series with predefined sizes

127   (nominal diameters).

128

129   **2.2 Experiments and sampling schedule**

130      Dried spherical PSL (Nanosphere Size Standards, Duke Scientific Corp., Palo Alto)

131   ($\rho_p$ = 1.055 g/cm$^3$ and $\chi$ = 1.0) with $D_{ve}$ values of 203.0 nm, 310.0 nm, 510.0 nm, and

132   740.0 nm were used in the AAC-SPAMS system. The PSL particles were first classified

133   by AAC, and then their $D_{va}$ values were obtained by SPAMS. ACC-SPAMS was also

134   applied to the particles of (NH$_4$)$_2$SO$_4$ ($\rho_p$ = 1.77 g/cm$^3$) and NaNO$_3$ ($\rho_p$ = 2.26 g/cm$^3$)

135   with $D_a$ values of 250.0 nm, 350.0 nm, 450.0 nm and 550.0 nm.

136      For field observations, the AAC-SPAMS system was placed in an urban area building

137   to characterize the $D_{ve}$, $\rho_e$ and chemical compositions of aerosol particles. The sampling

138   inlet was hung 2.5 meters from the third floor (~12 m above ground level). Ambient

139   aerosol particles were introduced into the AAC through a 5 m long conductive silicone

140   tube with an inner diameter of 6 mm and a PM$_{2.5}$ cyclone inlet. The overall sampling

141   flow was 3 L/min, and the residence time was approximately 5 seconds. Sampled

142   particles were classified by the AAC as one of four $D_a$: 250.0 nm, 350.0 nm, 450.0 nm

143   and 550.0 nm. The sampling time for the particles of each $D_a$ was approximately 10

144   minutes. From July 6th to 8th, 2019, approximately 100,000 ionized particles were

145    obtained. The sampling details are shown in Table S1.

146

**2.3 Theoretical derivation of $D_{ve}$ and $\rho_e$ from $D_a$ and $D_{va}$**

148    $D_{ve}$ is the accurate physical quantity of the size of a particle. $\rho_e$ is an alternative

149    property for $\rho_p$, which is consistent with the property of $\rho_p$ in terms of being independent

150    of particle size. These two properties cannot yet be measured for unknown particles by

151    current techniques. In this study, the calculations of $D_{ve}$ and $\rho_e$ for unknown particles

152    are theoretically derived from $D_a$ and $D_{va}$. Combining Eqs. (2) and (3), we obtain the

153    following Eq. (10):

$$C_{(D_a)}\frac{D_a{}^2}{D_{va}} = D_{ve}C_{(D_{ve})}\frac{\chi_v}{\chi_t} \tag{10}$$

155    Based on the approximation between $\chi_v$ and $\chi_t$ ($\chi_v \approx \chi_t = \chi_a$) (DeCarlo et al., 2004), Eq.

156    (10) becomes Eq. (11):

$$C_{(D_a)}\frac{D_a{}^2}{D_{va}} = D_{ve}C_{(D_{ve})} \tag{11}$$

158    If the $D_a$ and $D_{va}$ of an unknown particle can be measured, its $D_{ve}$ will be calculated

159    according to Eq. (11). Finally, the $\rho_e$ value of the particles is calculated by the $D_{va}$ and

160    $D_{ve}$ values according to Eq. (12):

$$\rho_e = \frac{\rho_p}{\chi_a} = \frac{D_{va}}{\rho_0 \cdot D_{ve}} \tag{12}$$

162    Thus, we can obtain both the $D_{ve}$ and $\rho_e$ values of unknown particles based on the $D_a$

163    and $D_{va}$ values. Because the AAC and SPAMS instruments have the ability to determine

164    $D_a$ and $D_{va}$, the AAC-SPAMS system, which is developed in this study, can be used to

165    obtain the $D_{ve}$ and $\rho_e$ values for unknown particles.

166

### 3. Results and discussion

#### 3.1 Verification of the AAC-SPAMS system to obtain $D_{ve}$ and $\rho_e$

169   The $D_{va}$ distribution of PSL particles with predefined $D_{ve}$ values after screening by

170   the AAC is shown in Figure S1. We used Gaussian fitting to obtain the peak $D_{va}$ for

171   each size PSL with an R-squared fitting coefficient ($R^2$) over 0.98. Each fitting has a

172   full width at half maximum (FWHM) of 6.6%, 4.4%, 2.3% and 2.2%, and the

173   corresponding peaks are 215.8 nm, 319.0 nm, 532.1 nm and 803.5 nm, respectively.

174   Substituting the $D_a$ and $D_{va}$ values of PSL into Eq. (11), the measured $D_{ve}$ ($D_{ve,me}$) of

175   PSL from AAC-SPAMS system is 203.6 nm, 309.7 nm, 511.6 nm and 737.2 nm,

176   respectively (Figure 2a). Thus, the deviations between the theoretical $D_{ve}$ ($D_{ve,th}$) and

177   $D_{ve,me}$ values are 0.3%, -0.1%, 0.3% and -0.4%, respectively. On the other hand, the

178   measured $\rho_e$ ($\rho_{e,me}$) values of the particles are calculated from the $D_{va}$ and $D_{ve,me}$ values

179   with Eq. (12), and the $\rho_{e,me}$ values are 1.06 g/cm$^3$, 1.03 g/cm$^3$, 1.04 g/cm$^3$, and 1.09

180   g/cm$^3$ (Figure 2b). Furthermore, based on a $\rho_p$ of 1.055 g/cm$^3$ and a $\chi$ of 1.0 for PSL

181   particles, the deviations of $\rho_{e,me}$ are 0.5%, -2.4%, -1.4%, and 3.3%, respectively. That

182   is, the deviations of $D_{ve,me}$ and $\rho_{e,me}$ characterized by the AAC-SPAMS system are within

183   1% and 4%, respectively. We therefore conclude that the AAC-SPAMS system is highly

184   accurate for obtaining aerosol $D_{ve}$ and $\rho_e$.

185

#### 3.2 Application of the AAC-SPAMS system for obtaining $D_{ve}$ and $\rho_e$ of $(NH_4)_2SO_4$ and $NaNO_3$

188   Figure S2 shows the $D_{va}$ distributions of $(NH_4)_2SO_4$ and $NaNO_3$ particles, which have

189    $D_a$ values of 250.0, 350.0, 450.0, and 550.0 nm, as screened by the AAC. The $D_{va}$ peaks

190    are obtained by Gaussian fitting, with $R^2$ values over 0.93 and FWHM values ranging

191    from 7.6% to 10.6%. The $(NH_4)_2SO_4$ particles have $D_{va}$ values of 300.0, 418.0, 551.1,

192    and 695.1 nm (Figure S2), which correspond to particles possessing $D_{ve,me}$ values of

193    177.3, 254.4, 331.8, and 409.3 nm, respectively, according to Eq. (11). Substituting the

194    values of $D_{va}$ and $D_{ve,me}$ into Eq. (12), the $\rho_{e,me}$ values are 1.74, 1.60, 1.65, and 1.74

195    g/cm$^3$ (Figure 3a), respectively. Similarly, the selected $NaNO_3$ particles are determined

196    to have $D_{va}$ values of 321.0, 454.9, 599.8, and 755.3 nm (Figure S2), corresponding to

197    $D_{ve,me}$ values of 150.1, 218.2, 287.0, and 355.9 nm, respectively. The $\rho_{e,me}$ values of the

198    $NaNO_3$ particles are 2.21, 2.03, 2.05, and 2.14 g/cm$^3$ for the four particle sizes (Figure

199    3b), respectively. Figure 3 also shows that the $\rho_{e,me}$ values of the $NaNO_3$ and $(NH_4)_2SO_4$

200    particles at four size slightly deviate from their average values, which are identical with

201    the deviation phenomenon for the $\rho_{e,me}$ of PSL particles. These deviations are derived

202    from the measurement of the particle $D_{va}$ in the SPAMS which size calibration curve

203    possesses the systematic error.

204        Taking the systematic error into account, the slight difference of the $\rho_{e,me}$ values for

205    the four sizes suggests that the $\rho_e$ of $(NH_4)_2SO_4$ and $NaNO_3$ particles is independent of

206    particle size from 250 nm to 550 nm. This pattern is divergent with the previous studies,

207    which showed that effective density decreased as the size increasing (Zelenyuk et al.,

208    2006; Zhang et al., 2016a). It is caused by the difference of the definitions of the

209    effective density. The definitions of effective density used in previous studies possessed

210    the inherent characteristics of decreasing with the increasing particle size, which will

211    be discussed in a separate paper. The definition of effective density used in this study

212    will keep constant as long as the $\chi_a$ of the particles does not change with particle size.

213    The average $\rho_{e,me}$ values of $(NH_4)_2SO_4$ and $NaNO_3$ particles are calculated to be $1.68 \pm$

214    $0.07$ and $2.11 \pm 0.08$ g/cm$^3$, respectively. The average $\rho_{e,me}$ values are lower than that

215    the $\rho_p$ of $(NH_4)_2SO_4$ (1.77 g/cm$^3$) and $NaNO_3$ (2.27 g/cm$^3$), which is caused that the

216    $\rho_{e,me}$ is determined by both of $\rho_p$ and $\chi_a$. According to Eq. (12), the $\chi_a$ of $(NH_4)_2SO_4$ and

217    $NaNO_3$ particles with different $D_a$ are calculated to be 1.02, 1.10, 1.07, and 1.02 and to

218    be 1.03, 1.12, 1.11, and 1.06, respectively. Thus, the average $\chi_a$ values of the $(NH_4)_2SO_4$

219    and $NaNO_3$ particles are determined to be $1.05 \pm 0.04$ and $1.08 \pm 0.04$, respectively,

220    which can be used to parameterize their morphology.

221      The average $\chi_a$ values of the $(NH_4)_2SO_4$ and $NaNO_3$ particles indicate that these

222    particles are aspherical. The asphericity of $(NH_4)_2SO_4$ determined by AAC-SPAMS

223    system is consistent with the previous studies reporting that the $\chi_a$ of $(NH_4)_2SO_4$ were

224    larger than the value of 1.03 (Zelenyuk et al., 2006; Beranek et al., 2012; Zhang et al.,

225    2016a). However, previous studies found that the $NaNO_3$ particles had different

226    morphology. Zhang et al. (2016a) observed that $NaNO_3$ had the $\chi_a$ of 1.09-1.13,

227    indicating its asphericity, while Hoffman et al. (2004) found that $NaNO_3$ particle had a

228    round droplet-like shape even at 15% RH, which was supported by the consistence

229    between the measured value of "anhydrous" droplet density and the calculated value of

230    "anhydrous" solution droplet (Zelenyuk et al., 2005). Eclectically, Tang and

231    Munkelwitz (1994) studied that most of the $NaNO_3$ particles crystallized between 20%

232    and 30% RH but some persisted down to 10% RH to form solution droplets. Notably,

233   the spherical NaNO$_3$ particles at low RH observed by Hoffman et al. (2004) were dried

234   in the sticky carbon tape which might affect the phase transition of droplet-like NaNO$_3$

235   particles. In this study, most NaNO$_3$ particles were crystallized because the RH of the

236   aerosol flow carrying the NaNO$_3$ particles was reduced to below 20% through the

237   diffusion drying tube. Besides, the result that the crystallized NaNO$_3$ particles are

238   aspherical is supported by their FWHM values of the $D_{va}$ distributions which are

239   consistent with that of aspherical (NH$_4$)$_2$SO$_4$ but different from spherical PSL (Figures

240   S1 and S2).

241

242   **3.3 Application of the AAC-SPAMS system for measuring the chemically-resolved**

243   **$D_{ve}$ and $\rho_e$**

244    SPAMS can obtain information on the chemical composition of individual particles,

245   implying that the AAC-SPAMS system has the ability to simultaneously characterize

246   $D_{ve}$, $\rho_e$ and the chemical compositions of particles in real time. It is worth noting that

247   the particles with the largest $\chi$ in the actual atmosphere should be freshly emitted soot,

248   which $\chi$ is 2.5 (Peng et al., 2016). This largest $\chi$ fitly meets the upper limit for the

249   approximation between the $\chi_t$ and $\chi_v$ (DeCarlo et al., 2004). Therefore, the AAC-SPAMS

250   system can obtain the chemically-resolved $D_{ve}$ and $\rho_e$ values for unknown aerosol

251   particles in the field observation.

252    As an example, we applied the AAC-SPAMS system to illustrate how the measured

253   $D_a$, $D_{va}$, and chemical composition of an individual particle can be used to calculate the

254   $D_{ve}$ and $\rho_e$ for unknown particles. The sampled ~100,000 particles are first classified by

255    using an adaptive resonance theory neural network (ART-2a) with a vigilance factor of

256    0.75, a learning rate of 0.05 and 20 iterations. The above system was used to cluster the

257    particles into eight major particle types with distinct chemical patterns of K-rich, EC-

258    S, K-Na, Amine, EC-N-S, OC-N-S and OC-EC-N-S and Metal-rich, representing 97%

259    of the detected particle population. Details of the chemical composition and number

260    fraction of the eight types of particles are provided in the Supporting Information.

261    We used Gaussian fitting to obtain the $D_{va}$ peaks for each particle type with $D_a$ values

262    of 250.0 nm, 350.0 nm, 450.0 nm, and 550.0 nm. Then, we calculated the $D_{ve}$ values of

263    the atmospheric particles with Eq. (11). Table 1 presents the average $D_{ve}$ values of the

264    eight particle types, for which the standard deviation is calculated based on nine

265    samples. The average $D_{ve}$ at $D_a$ values of 250.0 nm, 350.0 nm, 450.0 nm, and 550.0 nm

266    has the following wide ranges: from 188.5 nm to 200.8 nm, 271.9 nm to 295.7 nm,

267    342.5 nm to 428.9 nm, and 397.3 nm to 570.9 nm, respectively, which are caused by

268    the chemical composition differences. The result indicates that particles with

269    significantly different $D_{ve}$ might possess the same $D_a$. Furthermore, the large standard

270    deviation of $D_{ve}$, such as 21.9 nm for K-Na at 250.0 nm, 32.3 nm for OC-EC-N-S at

271    350.0 nm, and 44.3 nm for OC-N-S at 450.0 nm, indicates that the $D_{ve}$ of particles is

272    remarkably different even for particles with the same type and same $D_a$.

273    According to $D_{ve}$ and $D_{va}$, we calculated the $\rho_e$ of each particle type with Eq. (12).

274    Figure 4 shows the variations of the $\rho_e$ with $D_{ve}$ for nine particle samples. For pure

275    compounds, such as $(NH_4)_2SO_4$ and $NaNO_3$ particle, $\rho_e$ theoretically does not change

276    with particle size. However, the sampled particles have experienced complex

277    atmospheric processes. Therefore, $\rho_e$ has a very wide distribution for each type of

278    particle with a similar $D_{ve}$. Specifically, the $\rho_e$ of K-Na increases with $D_{ve}$, while the $\rho_e$

279    of OC-N-S and OC-EC-N-S decreases with $D_{ve}$, which may be influenced by the

280    particle shape. Additionally, the average $\rho_e$ of each type of particle is in the order from

281    small to large: $1.21 \pm 0.20$ g/cm$^3$ for OC-EC-N-S, $1.25 \pm 0.15$ g/cm$^3$ for OC-N-S, 1.45

282    $\pm 0.06$ g/cm$^3$ for K-rich, $1.45 \pm 0.04$ g/cm$^3$ for Amine, $1.46 \pm 0.05$ g/cm$^3$ for EC-N-S,

283    $1.47 \pm 0.02$ g/cm$^3$ for EC-S, $1.55 \pm 0.09$ g/cm$^3$ for K-Na and $1.56 \pm 0.08$ g/cm$^3$ for

284    Metal-rich. It is reasonable to find that the average $\rho_e$ of internally mixed particles

285    distributes in the range of their material densities ($\rho_m$). For instance, mainly comprised

286    of internally mixed sulfate and organics, the OC-EC-N-S, OC-N-S, K-rich, and Amine

287    particles have the average $\rho_e$ between that of sulfate with $\rho_m$ of 1.77 g/cm$^3$ and organic

288    aerosols with $\rho_m$ of 1.2 g/cm$^3$ (Cross et al., 2007).

289

290    **4. Conclusion**

291       We first develop an AAC-SPAMS system to achieve the measurement of the $D_{ve}$ and

292    $\rho_e$ of the particles through characterizing their $D_a$ and $D_{va}$. The reliability of the AAC-

293    SPAMS system is verified by accurately measuring the $D_{ve}$ and $\rho_e$ of PSL. Applying the

294    AAC-SPAMS system to determine the $D_{ve}$ and $\rho_e$ of $(NH_4)_2SO_4$ and $NaNO_3$ particles

295    shows that these particles are aspherical and their $\rho_e$ are independent of particle size.

296    Coupled with the ability of SPAMS to characterize the chemical composition of

297    individual particles, we conducted a sample proof of the AAC-SPAMS equipment in

298    Guangzhou to first characterize the $D_{ve}$, $\rho_e$ and chemical compositions of atmospheric

299    particles, showing the potential application of this system in field observations. The

300    approach achieves the measurement of chemically-resolved $D_{ve}$ and $\rho_e$, and provides

301    the possibility to determine their quantitative relationship with other particle properties,

302    which would be benefit for further reduction of the uncertainty associated with the

303    effects of particles on air quality, human health and radiative forcing.

304

305    *Data availability.* Data in this study is available at https://github.com/longer1217/All-

306    figures-data.

307

308    *Author contributions.* The idea for the study was conceived by LP and GHZ. All

309    experiments were performed by LP with the assistance of LL. LP wrote the paper which

310    was reviewed by GHZ and XHB. All co-authors discussed the results and commented

311    on the manuscript.

312

313    **Competing interests.** The authors declare they have no conflict of interest.

314

315    **Acknowledgment**

316    This work was supported by the National Nature Science Foundation of China

317    (41775124 and 41877307), Natural Science Foundation of Guangdong Province

318    (2019B151502022), and the Guangdong Foundation for the Program of Science and

319    Technology Research (2019B121205006 and 2017B030314057). The authors also

320    gratefully acknowledge Cambustion Ltd., UK for providing the AAC and Hexin

321    Analytical Instrument Co., Ltd., China for providing the  SPAMS.

322

323    **References**

324    Beranek, J., Imre, D., and Zelenyuk, A.: Real-time shape-based particle separation and

325        detailed in situ particle shape characterization, Anal. Chem., 84, 1459-1465,

326        https://doi.org/10.1021/ac202235z, 2012.

327    Buseck, P. R., and Posfai, M.: Airborne minerals and related aerosol particles: Effects

328        on climate and the environment, P. Natl. Acad. Sci. USA, 96, 3372-3379,

329        https://doi.org/10.1073/pnas.96.7.3372, 1999.

330    Cross, E. S., Slowik, J. G., Davidovits, P., Allan, J. D., Worsnop, D. R., Jayne, J. T.,

331        Lewis, D. K., Canagaratna, M., and Onasch, T. B.: Laboratory and ambient particle

332        density determinations using light scattering in conjunction with aerosol mass

333        spectrometry,    Aerosol    Sci.    and    Technol.,    41,    343-359,

334        https://doi.org/10.1080/02786820701199736, 2007.

335    DeCarlo, P. F., Slowik, J. G., Worsnop, D. R., Davidovits, P., and Jimenez, J. L.: Particle

336        morphology and density characterization by combined mobility and aerodynamic

337        diameter measurements. Part 1: Theory, Aerosol Sci. and Technol., 38, 1185-1205,

338        https://doi.org/10.1080/027868290903907, 2004.

339    Guo, S., Hu, M., Zamora, M. L., Peng, J. F., Shang, D. J., Zheng, J., Du, Z. F., Wu, Z.,

340        Shao, M., Zeng, L. M., Molina, M. J., and Zhang, R. Y.: Elucidating severe urban

341        haze formation in China, P. Natl. Acad. Sci. USA, 111, 17373-17378, 2014.

342    Hoffman, R. C., Laskin, A., and Finlayson-Pitts, B. J.: Sodium nitrate particles: physical

343      and chemical properties during hydration and dehydration, and implications for

344      aged sea salt aerosols, J. Aerosol Sci., 35, 869-887, 2004.

345      Katrib, Y., Martin, S. T., Rudich, Y., Davidovits, P., Jayne, J. T., and Worsnop, D. R.:

346      Density changes of aerosol particles as a result of chemical reaction, Atmos. Chem.

347      Phys., 5, 275-291, https://doi.org/10.5194/acp-5-275-2005, 2005.

348      Li, L., Huang, Z. X., Dong, J. G., Li, M., Gao, W., Nian, H. Q., Fu, Z., Zhang, G. H.,

349      Bi, X. H., Cheng, P., and Zhou, Z.: Real time bipolar time-of-flight mass

350      spectrometer for analyzing single aerosol particles, Int. J. Mass Spectrom., 303,

351      118-124, https://doi.org/10.1016/j.ijms.2011.01.017, 2011.

352      Liu, Y., and Daum, P. H.: Relationship of refractive index to mass density and self-

353      consistency of mixing rules for multicomponent mixtures like ambient aerosols, J.

354      Aerosol Sci., 39, 974-986, https://doi.org/10.1016/j.jaerosci.2008.06.006, 2008.

355      Liu, Z., Hu, B., Ji, D., Wang, Y., Wang, M., and Wang, Y.: Diurnal and seasonal variation

356      of the PM2.5 apparent particle density in Beijing, China, Atmos. Environ., 120,

357      328-338, https://doi.org/10.1016/j.atmosenv.2015.09.005, 2015.

358      Moffet, R. C., and Prather, K. A.: Extending ATOFMS measurements to include

359      refractive index and density, Anal. Chemis., 77, 6535-6541,

360      https://doi.org/10.1021/ac0503097, 2005.

361      Peng, J. F., Hu, M., Guo, S., Du, Z. F., Zheng, J., Shang, D. J., Zamora, M., Zeng, L.

362      M., Shao, M., Wu, Y. S., Zheng, J., Wang, Y., Glen, C., Collins, D., Molina, M.,

363      and Zhang, R. Y.: Markedly enhanced absorption and direct radiative forcing of

364      black carbon under polluted urban environments, P. Natl. Acad. Sci. USA, 113,

365    4266–4271, 2016.

366    Pitz, M., Cyrys, J., Karg, E., Wiedensohler, A., Wichmann, H. E., and Heinrich, J.:

367        Variability of apparent particle density of an urban aerosol, Environ. Sci. &

368        Technol., 37, 4336-4342, https://doi.org/10.1021/es034322p, 2003.

369    Poschl, U.: Atmospheric aerosols: Composition, transformation, climate and health

370        effects, Angew. Chem. Int. Edit., 44, 7520-7540,

371        https://doi.org/10.1002/anie.200501122, 2005.

372    Seinfeld, J. H., and Pandis, S. N.: From air pollution to climate change, 429-443, 1998.

373    Sumlin, B. J., Oxford, C. R., Seo, B., Pattison, R. R., Williams, B. J., and Chakrabarty,

374        R. K.: Density and homogeneous internal composition of primary brown carbon

375        aerosol, Environ. Sci. & Technol., 52, 3982-3989,

376        https://doi.org/10.1021/acs.est.8b00093, 2018.

377    Tang, I. N., and Munkelwitz, H. R.: Water Activities, Densities, and Refractive-Indexes

378        of Aqueous Sulfates and sodium-nitrate droplets of atmospheric importance, J.

379        Geophys. Res.-Atmos., 99, 18801-18808, 1994.

380    Tang, I. N.: Thermodynamic and optical properties of mixed-salt aerosols of

381        atmospheric importance, J. Geophys. Res.-Atmos., 102, 1883-1893, 1997.

382    Tavakoli, F., and Olfert, J. S.: An instrument for the classification of aerosols by particle

383        relaxation time: Theoretical models of the aerodynamic aerosol classifier, Aerosol

384        Sci. and Technol., 47, 916-926, https://doi.org/10.1080/02786826.2013.802761,

385        2013.

386    Yin, Z., Ye, X. N., Jiang, S. Q., Tao, Y., Shi, Y., Yang, X., and Chen, J. M.: Size-resolved

387    effective density of urban aerosols in Shanghai, Atmos. Environ., 100, 133-140,

388    https://doi.org/10.1016/j.atmosenv.2014.10.055, 2015.

389   Yon, J., Bescond, A., and Ouf, F. X.: A simple semi-empirical model for effective

390    density measurements of fractal aggregates, J. Aerosol Sci., 87, 28-37,

391    https://doi.org/10.1016/j.jaerosci.2015.05.003, 2015.

392   Zelenyuk, A., Cai, Y., Chieffo, L., and Imre, D.: High precision density measurements

393    of single particles: The density of metastable phases, Aerosol Sci. and Technol.,

394    39, 972-986, https://doi.org/10.1080/02786820500380206, 2005.

395   Zelenyuk, A., Cai, Y., and Imre, D.: From agglomerates of spheres to irregularly shaped

396    particles: Determination of dynamic shape factors from measurements of mobility

397    and vacuum aerodynamic diameters, Aerosol Sci. and Technol., 40, 197-217,

398    https://doi.org/10.1080/02786820500529406, 2006.

399   Zhang, G., Bi, X., Han, B., Qiu, N., Dai, S., Wang, X., Sheng, G., and Fu, J.:

400    Measurement of aerosol effective density by single particle mass spectrometry,

401    Science China Earth Sciences, 59, 320-327, https://doi.org/10.1007/s11430-015-

402    5146-y, 2016a.

403   Zhao, G., Zhao, W., and Zhao, C.: Method to measure the size-resolved real part of

404    aerosol refractive index using differential mobility analyzer in tandem with single-

405    particle    soot    photometer,    Atmos.    Meas.    Tech.,    12,    3541-3550,

406    https://doi.org/10.5194/amt-12-3541-2019, 2019.

407 **Table 1.** $D_{ve}$ for the eight particle types at $D_a$ values of 250.0 nm, 350.0 nm, 450.0 nm, and 550.0
408 nm
409

| $D_a$ (nm) | K-rich | EC-S | K-Na | Amine |
|---|---|---|---|---|
| **250.0** | 193.1 ± 8.2 | 192.2 ± 8.1 | 193.8 ± 21.9 | 190.6 ± 4.6 |
| **350.0** | 284.0 ± 28.4 | 280.8 ± 9.3 | 271.9 ± 18.0 | 284.8 ± 18.2 |
| **450.0** | 364.7 ± 21.1 | 357.8 ± 6.9 | 342.5 ± 7.3 | 367.9 ± 9.7 |
| **550.0** | 416.6 ± 28.3 | 439.5 ± 5.4 | 397.3 ± 29.7 | 442.5 ± 7.4 |
| $D_a$ (nm) | EC-N-S | OC-N-S | OC-EC-N-S | Metal-rich |
| **250.0** | 188.5 ± 5.9 | 200.8 ± 17.9 | 195.4 ± 8.9 | 189.0 ± 6.7 |
| **350.0** | 281.3 ± 9.3 | 295.7 ± 29.8 | 294.0 ± 32.3 | 277.0 ± 9.1 |
| **450.0** | 358.0 ± 5.8 | 398.3 ± 44.3 | 428.9 ± 24.0 | 342.9 ± 10.0 |
| **550.0** | 453.2 ± 16.4 | 547.4 ± 14.7 | 570.9 | 407.4 ± 14.5 |

410
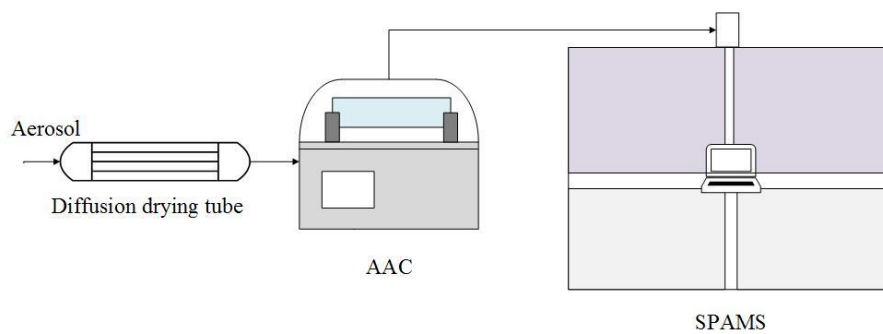
411

412        **Figure 1.** Schematic diagram of the AAC-SPAMS system.
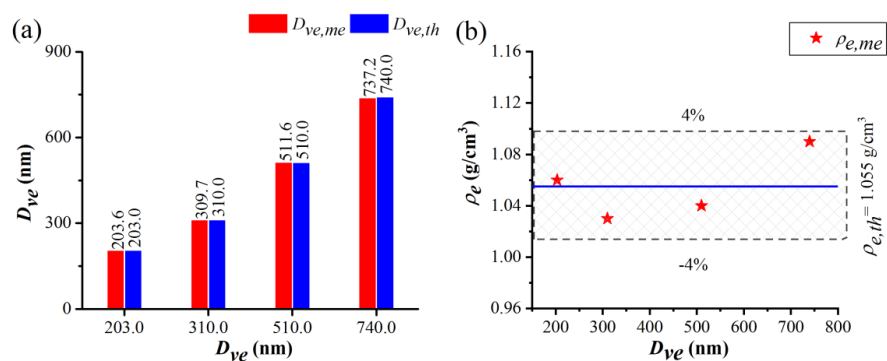
413

414

415    **Figure 2.** (a) Comparison between the measured $D_{ve}$ ($D_{ve,me}$) and the theoretical $D_{ve}$ ($D_{ve,th}$) of the

416    PSL particles. (b) Comparison between the measured $\rho_e$ ($\rho_{e,me}$) and the theoretical $\rho_e$ ($\rho_{e,th}$) of the

417    PSL particles.
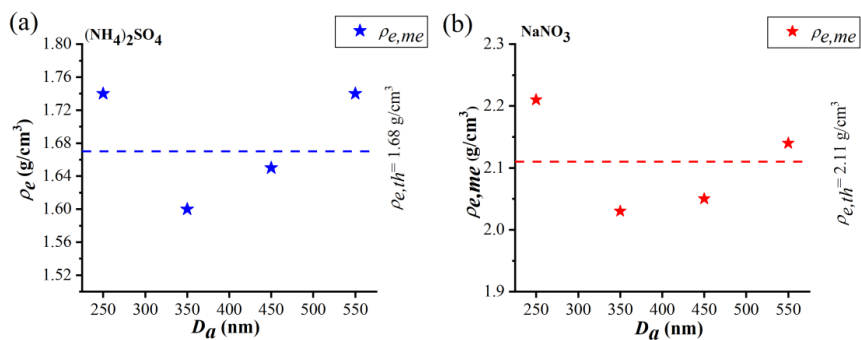
418

419 **Figure 3.** (a) Comparison between the measured $\rho_e$ ($\rho_{e,me}$) and theoretical $\rho_e$ ($\rho_{e,th}$) values of the

420 $(NH_4)_2SO_4$ particles. (b) Comparison between the measured $\rho_e$ ($\rho_{e,me}$) and theoretical $\rho_e$ ($\rho_{e,th}$) values

421 of the $NaNO_3$ particles.
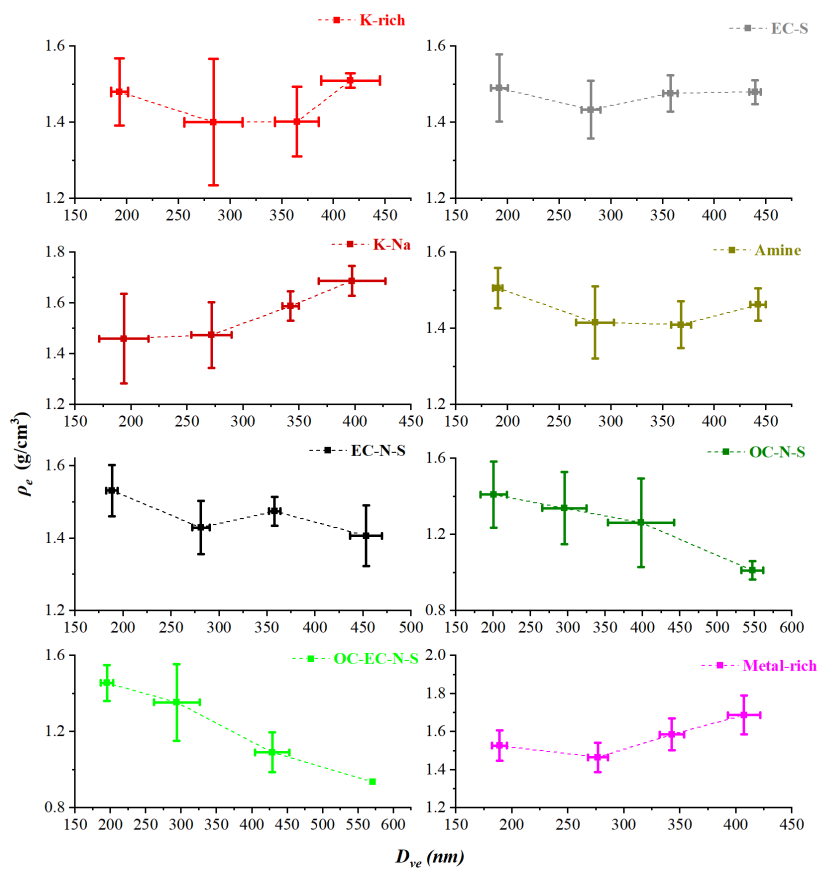
422

423

424            **Figure 4.** Variation in $\rho_e$ of the eight particle types with $D_{ve}$.